Dislocation-mediated electronic conductivity in rutile

Qaisar Khushi Muhammad, Hanna Bishara, Lukas Porz, Christian Dietz, Matteo Ghidelli, Gerhard Dehm, Till Frömling

To cite this version:

Qaisar Khushi Muhammad, Hanna Bishara, Lukas Porz, Christian Dietz, Matteo Ghidelli, et al.. Dislocation-mediated electronic conductivity in rutile. Materials Today Nano, 2022, 17, pp.100171. 10.1016/j.mtnano.2021.100171 . hal-03542369

Dislocation-mediated electronic conductivity in rutile

Qaisar Khushi Muhammad[a,*], Hanna Bishara[b], Lukas Porz[a], Christian Dietz[c], Matteo Ghidelli[b,d], Gerhard Dehmb and Till Frömling[a,*]

[a]Division of Nonmetallic-Inorganic Materials, Department of Materials and Earth Sciences, Technical University of Darmstadt, Alarich-Weiss-Str. 2, Darmstadt, 64287, Germany

[b] Department of Structure and Nano-/Micromechanics of Materials Thin Layers & Nanostructured Materials, Max-Planck-Institut für Eisenforschung GmbH, Max-Planck-Str. 1, Düsseldorf, 40237, Germany

[c] Division of Physics of Surfaces, Department of Materials and Earth Sciences, Technical University of Darmstadt, Alarich-Weiss-Str. 2, Darmstadt, 64287, Germany

[d]Laboratoire des Sciences des Procédés et des Matériaux (LSPM), CNRS, Université Sorbonne Paris Nord, 93430, Villetaneuse, France

*Corresponding authors:
Froemling@ceramics.tu-darmstadt.de;
muhammad@ceramics.tu-darmstadt.de
Fax: +49 6151 16-21695

Abstract

It has been recently shown that doping-like properties can be introduced into functional ceramics by inducing dislocations. Especially for TiO_2, donor and acceptor-like behavior were observed depending on the type of introduced mesoscopic dislocation network. However, these early reports could not fully elucidate the mechanism behind it. In this work, we rationalize the electrical properties of dislocations by targeted microelectrode measurements on deformed single crystals, comparing dislocation-rich and deficient regions. With the help of finite element method (FEM) calculations, a semi-quantitative model for the effect of dislocations on the macroscopic electrical properties is developed. The model describes the dislocation bundles as highly conductive regions in which respective space charges overlap and induce temperature-independent, highly stable electronic conductivity. We illustrate the mechanism behind unique electrical properties tailored by introducing dislocations and believe that these results are the cornerstone in developing dislocation-tuned functionality in ceramics.

Teaser (as per journal format requirement/**NOT** part of the main text)

The field of dislocation-tuned functionality came onto the scene about eight years ago. It took few years to develop as it involves a fundamental understanding of both chemistry and mechanics and dedicated characterization. However, this year may be the breakthrough for this field with devices ultimately based on atomic-scale functionality. It will be a completely new materials paradigm, i.e., new devices not made by ***atomistic doping*** *but by* ***mechanical or 1-dimensional doping****. We believe that our work provides a critical understanding of the newly coined dislocation-tuned electrical conductivity in ceramics.*

1. Introduction

While the research on dislocation-based functionality in metal oxides and semiconductors is still in its infancy (*1, 2*), the high potential to tune properties of ceramics by dislocations was already illustrated decades ago (*3*). A dislocation is a one-dimensional (extended) defect that possesses a large elastic strain field around its core region (*4*). Furthermore, dislocations in ceramics can be charged depending on its core structure due to the lattice's ionic nature (*3, 5, 6*). This gives dislocations the potential to induce peculiar physical properties and the ability to modify the functionality of ceramics, such as electrical conductivity (*7-9*), thermal conductivity (*10-12*), and ferroelectric properties (*13*).

Nevertheless, ceramics are regarded as brittle materials, and the controlled introduction of dislocations is rather challenging (*14*). Therefore, the control of dislocations in order to tune the functional properties of ceramic has been mostly ignored in the past. However, the understanding of the potential to introduce dislocations into ceramics is now developing with promising recent examples on, e.g., $SrTiO_3$ (*1, 15*), MgO (*2*), and ZnS (*16, 17*). To induce dislocations in ceramics, several endeavors are feasible, including the fabrication of bi-crystals (*18-20*), indentation (*21, 22*), and surface polishing (*23*). However, the most reproducible method for controlling the natural mesoscopic dislocation structure is uniaxial deformation (*24*). Single crystals can be plastically deformed as a function of temperature, promoting the activation of favorable slip systems resulting in dense dislocation networks (*14, 24*). This makes this method broadly applicable at high temperatures (*12, 25, 26*) and for some ceramics even at room temperature (*16, 17, 27-29*).

Recently, dislocations have been described by Adepalli *et al.* as "one-dimensional dopants" to improve the electrical conductivity of single and polycrystalline rutile (*30, 31*). However, a non-controlled mesoscopic dislocations structure was utilized in this case. In our previous work on rutile, dislocation arrangement (slip systems/recovery behavior) alongside their impact on macroscopic electrical conductivity was reported (*32*). Controlled mesoscopic dislocation structures were introduced above the recovery temperature (1020 °C). This particular deformation temperature was chosen, as above this temperature, dislocation climb becomes active. This leads to dislocations aligning themselves due to their train fields in the form of bundles on favorable planes leaving behind a dislocation-free (recovered) zone (*33*). These bundle-like dislocation configurations were found responsible for the increase in electrical conductivity (*32*). Oxygen partial pressure (pO_2) dependent electrical measurements (ambient to 10^{-5} bar) provided evidence that rutile samples deformed above 1020 °C behave like donor-doped samples compared to undeformed material (*32*).

Surprisingly, in the temperature-dependent measurements, there is no significant change in the activation energy of conductivity. This was rationalized by assuming that dislocations increase the electronic conductivity due to the adjacent space charge. However, no dislocation network develops, connecting the electrodes through the whole sample (*32*). Therefore, there is still a contribution of conduction through the bulk material in series to the dislocation conduction. The conductive path was proposed with "small gaps" in it, having a key role. The behavior of the gap then ultimately dominated the temperature dependence of conductivity (*32*). Even though this hypothesis certainly fits the obtained results, more evidence or at least a semi-quantitative description is required to fully elucidate the effect of dislocations. Furthermore, these studies considered dislocation doping effects on electrical conductivity only at elevated temperatures, which limits the effective use of reported conductivity to the key applications of TiO_2 at/near ambient temperature (*30, 32*).

In the present work, dislocation-rich bundles and recovered (dislocation-free/deficient) regions are investigated separately by means of microcontact impedance spectroscopy. This allows rationalizing the contribution of different areas with varying dislocation density independently (implausible with bulk measurements). The data interpretation is also supported by FEM calculations, resulting in a semi-quantitative description of the impact of dislocations and their arrangement on the conductivity. A comprehensive correlation is made between mesoscopic dislocation structure, arrangement, density, and enhanced local electrical conductivity to deconvolute the dislocation behavior as dopants in rutile.

2. Results and Discussion

2.1. Mesoscopic dislocation arrangement

Uniaxial compression along [c-010] direction at 1050 °C (under ambient conditions) activated the predominant {011} <011> slip system at an angle of 57.27°. The maximum Schmid factor is obtained when deforming along the [010] direction (Fig. 2A/S1A-C). The deformed single crystals were cut at an angle of 45°, resulting in (120) surface planes. The dislocation lines moving onto (011) planes intersect the (120) planes at an angle of ≈ 20° (Fig. 2A). These dislocation lines are then visualized on the (120) plane in the form of etch-pits *via* chemical etching. Dislocation recovery behavior is observed as dislocation bundles are formed, leaving recovered zones between these bundles, and the dislocation density is remarkably reduced in the recovered zones (Figs. 2A-B). In a previous publication, it could be shown that this behavior is prevalent at temperatures above 1020 °C while evenly distributed dislocations are induced below this temperature (*32*). Thus, an arranged and highly dense mesoscopic dislocation structure is attained in these bundles. This allows local electrical investigations on dislocation-rich (bundles) and dislocation deficient (recovered) areas on the same sample (Fig. 2C).

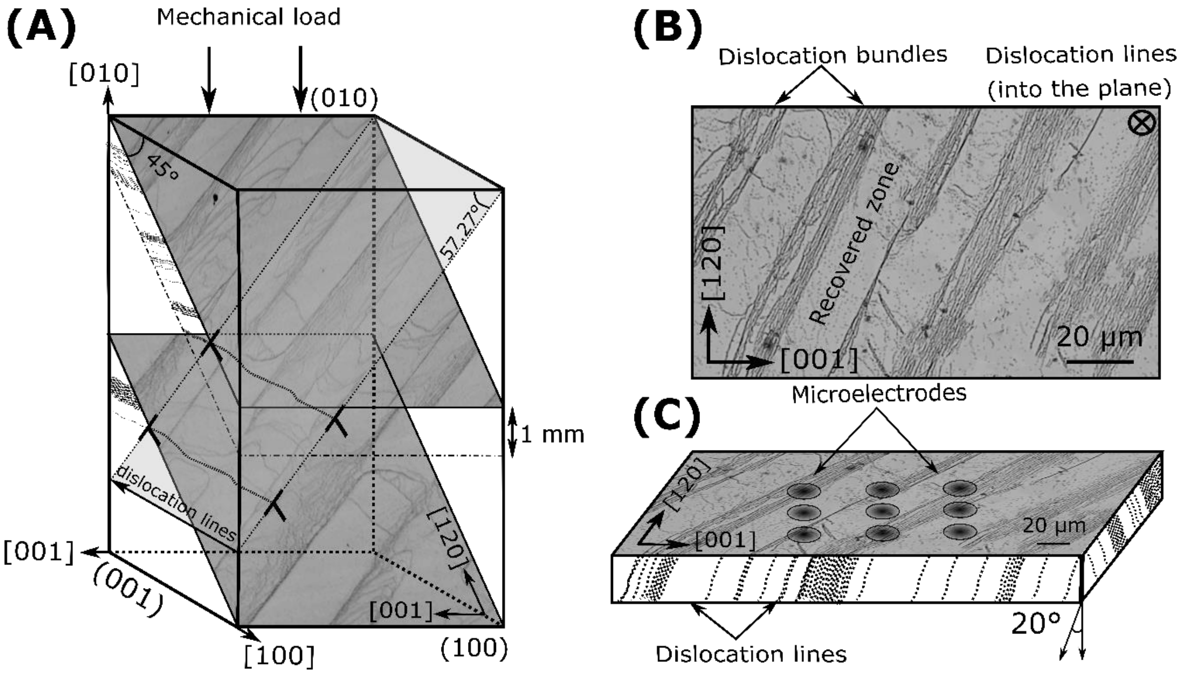

Fig. 2. Conceptualization of experimental design. (**A**) schematic of crystal orientation and loading direction of rutile single crystals (along with activated predominant {011} <011> slip system at an angle of 57.27° with the (010) plane, highlighted in dotted grey (also see Fig. **S1A**). Laser microscope images of chemically etched (120) planes of exactly the same region are presented, recovery behavior can be observed onto the etched planes. Dislocation lines move on the (011) plane in the direction of [100], intersecting (120) plane at an angle, dislocations are visualized as etch-pits onto (120) planes. (**B**) front view of 1 mm thick specimen with etched (120) plane extracted from (**A**), mesoscopic dislocation structure is perceptible at higher magnification while dislocation lines going into the plane (symbol ⊗), recovered zone, and dislocation bundles are optically rationalized. (**C**) schematic of the same specimen in (**B**) with actual micrograph on the top (dislocation lines go through the sample at an angle of ≈ 20°) along with the schematic of targeted microelectrodes onto the dislocation bundles as well as the recovered zone.

To compare local electrical properties, microelectrodes were accurately placed onto the recovered region and the dislocation bundles (Figs. 3A-C). Photolithography (details in supplemental) and physical vapor deposition (PVD) was employed to obtain Al-Au microelectrodes in the recovered zone (low dislocation density) ($E_{PVD\text{-}1}$), bundled regions with medium ($E_{PVD\text{-}2}$), and high dislocation density ($E_{PVD\text{-}3}$) areas. Figs. 3D-F presents SEM images of selected microelectrodes where dislocation arrays beneath the microelectrodes are visible. HR-SEM (Fig. 3G) made it possible to quantify the number of dislocations underneath the selected microelectrodes. It was confirmed that $E_{PVD\text{-}1}$ in Fig. 3A is placed in the recovered zone or simply in a very low dislocation density region (roughly 40 ± 5 etch pits). Whereas 2800 and 4000 (± 50) etch pits were found under $E_{PVD\text{-}2}$ and $E_{PVD\text{-}3}$, respectively.

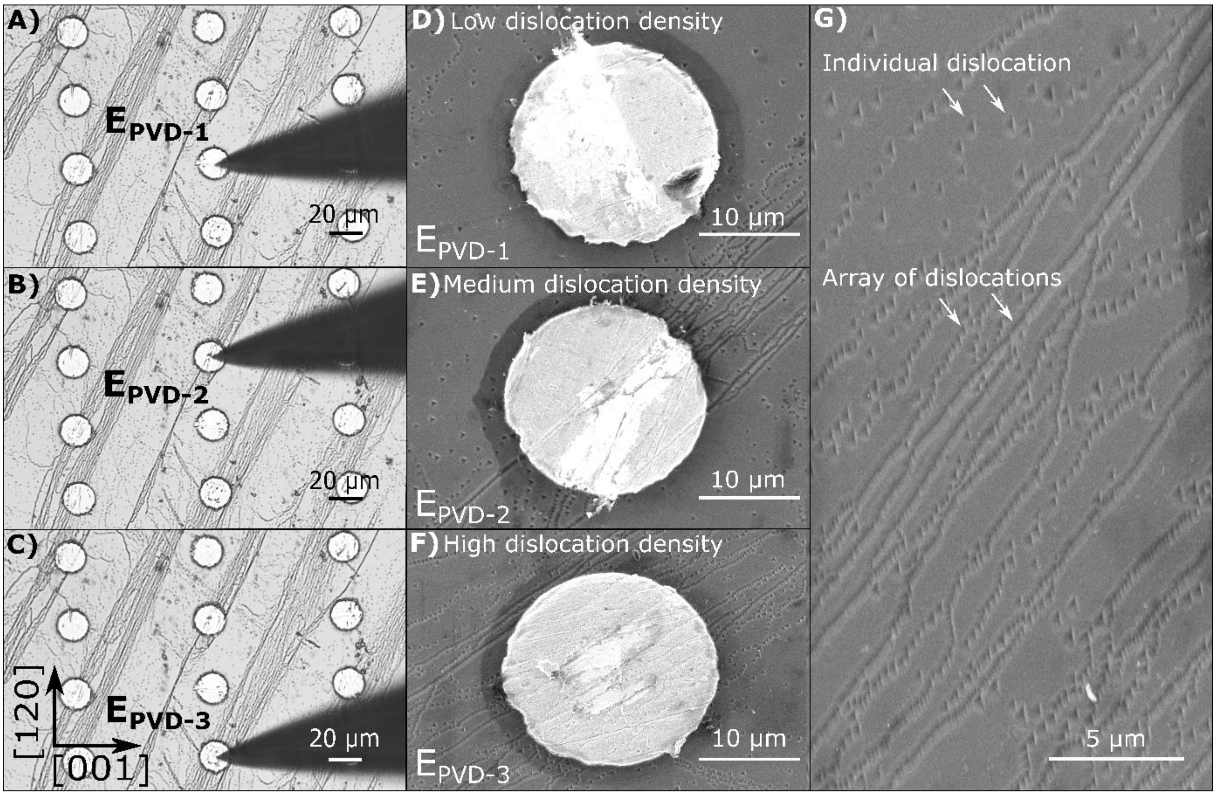

Fig. 3. Arranged mesoscopic dislocation structure and microelectrodes. (**A-C**) Laser microscope images of the specimens with Al-Au microelectrodes of 20 µm diameter. E_{PVD-1}, E_{PVD-2}, and E_{PVD-3} represent recovered zone, bundled regions with medium and high dislocation density, respectively. (**D-F**) Scanning Electron Microscope (SEM) images of microelectrodes furnished in the recovered zone (low dislocation density) E_{PVD-1}, bundled regions with medium (E_{PVD-2}), and high dislocation density (E_{PVD-3}). (**G**) high-resolution SEM image of the same sample before deposition of the microelectrodes depicts etch-pits from the mesoscopic dislocation structure.

2.2. Electrical characterization/Microcontact impedance spectroscopy (MCIS)

Low (E_{PVD-1}), medium (E_{PVD-2}), and high dislocation density (E_{PVD-3}) areas are probed *via* tungsten needles by means of impedance spectroscopy (Fig. 4A). Fig. 4B features impedance spectra experimentally recorded at room temperature for all three regions. During microcontact probing, the voltage is applied between a circular microelectrode and a large bottom counter-electrode comparatively far away from this microelectrode. Therefore, it is expected that the voltage drops very close to the microelectrode and allows for obtaining local resistance information (*34*). The conductive pathways of dislocations can change this situation fundamentally, though. This is illustrated for simulations emulating the low-temperature behavior in Fig. 1 (see Materials and Methods section). There, the high conductivity of the dislocations compared to the bulk leads to a major voltage drop at the gap between two dislocation bundles instead of directly below the electrode.

Qualitative information on the different resistance between the regions of varying dislocation density can be obtained, which indicates the size scale-dependent behavior. For the dislocation deficient region (E_{PVD-1}), one semicircle is observed while no further process can be resolved at high or low frequencies (Figs. 4B-C). This represents the single electrical process with a capacitance in the range of 2×10^{-12} F. Therefore, this electrical response can be attributed to the bulk process (*35*). For E_{PVD-2} and E_{PVD-3}, two different semicircles and thus two resistive responses can be determined. However, the high-frequency response only becomes visible in Fig. 4C, which focuses on the high-frequency data. These two processes could be attributed to the dislocations and the bulk response. Furthermore, orders of magnitude difference is observed between the dislocation-deficient region response (E_{PVD-1}) and the first electrical response of the areas with dislocation bundles (E_{PVD-2}). The reduction in resistance of the first electrical response becomes even more pronounced with a higher density of dislocation bundles E_{PVD-3} (Figs. 3F/4C). We note that over 100 different microelectrodes were measured at room temperature to have statistically reliable data, while in Fig. 4, we report a representative set of measurements.

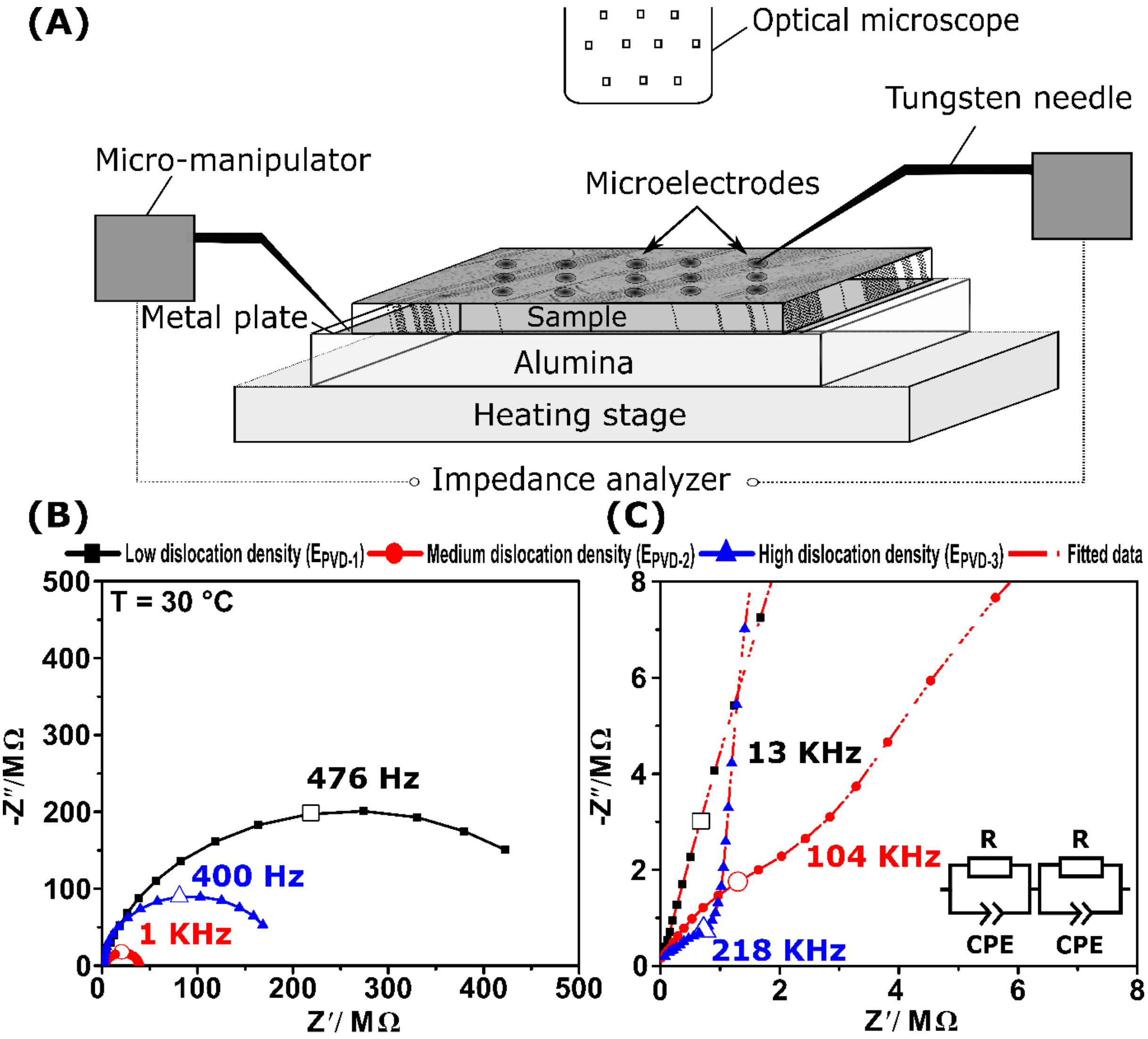

Fig. 4. Microcontact impedance spectroscopy (PVD deposited electrodes). (**A**) Schematic of the microcontact impedance setup depicting heating stage, alumina case, and the sample. The actual micrograph is presented along with the schematic of microelectrodes. Two-probe measurement setup is employed; one tungsten needle is used to probe upper microelectrodes while the other contacts the large metal plate at the bottom electrode. (**B**) Nyquist plots of impedance for selected microelectrodes (at room temperature); onto low (E_{PVD-1}), medium (E_{PVD-2}), and high dislocation density areas (E_{PVD-3}), (AC frequency values are labeled at the capacitance maxima). No Schottky barrier is observed within the measurement frequency range. (**C**) Aside from the bulk response visible for all three electrodes, E_{PVD-2} and E_{PVD-3} show an additional process at high frequencies attributed to the dislocations. Measured data could be fitted using the equivalent circuit presented in the inset.

To expand investigations down to a very local scale, further impedance measurements are performed onto "electron beam assisted-gas injection system" (GIS) deposited minuscule microcontacts (only possible inside an SEM chamber; details in supplemental). Figs. 5A-C presents SEM images of GIS deposited 3 × 3 μm^2 tungsten microelectrodes (onto another slice of the same deformed crystal). To ensure the data presentation consistency, we distinguish these microelectrodes by low (E_{GIS-1}), medium (E_{GIS-2}), and high dislocation density (E_{GIS-3}) areas. One may argue about the impact of vacuum and electron beam inside the SEM chamber on measured electrical conductivity. A comparison between out and inside SEM measurements is made to address this, which conferred no difference in impedance spectra. Furthermore, another experimental comparison is made between the electron beam "OFF" and "ON" inside the SEM chamber. This results in overlap of impedance spectra and confirms that measurements inside the SEM chamber with the electron beam "switched ON" produce reliable results (see Fig. S4).

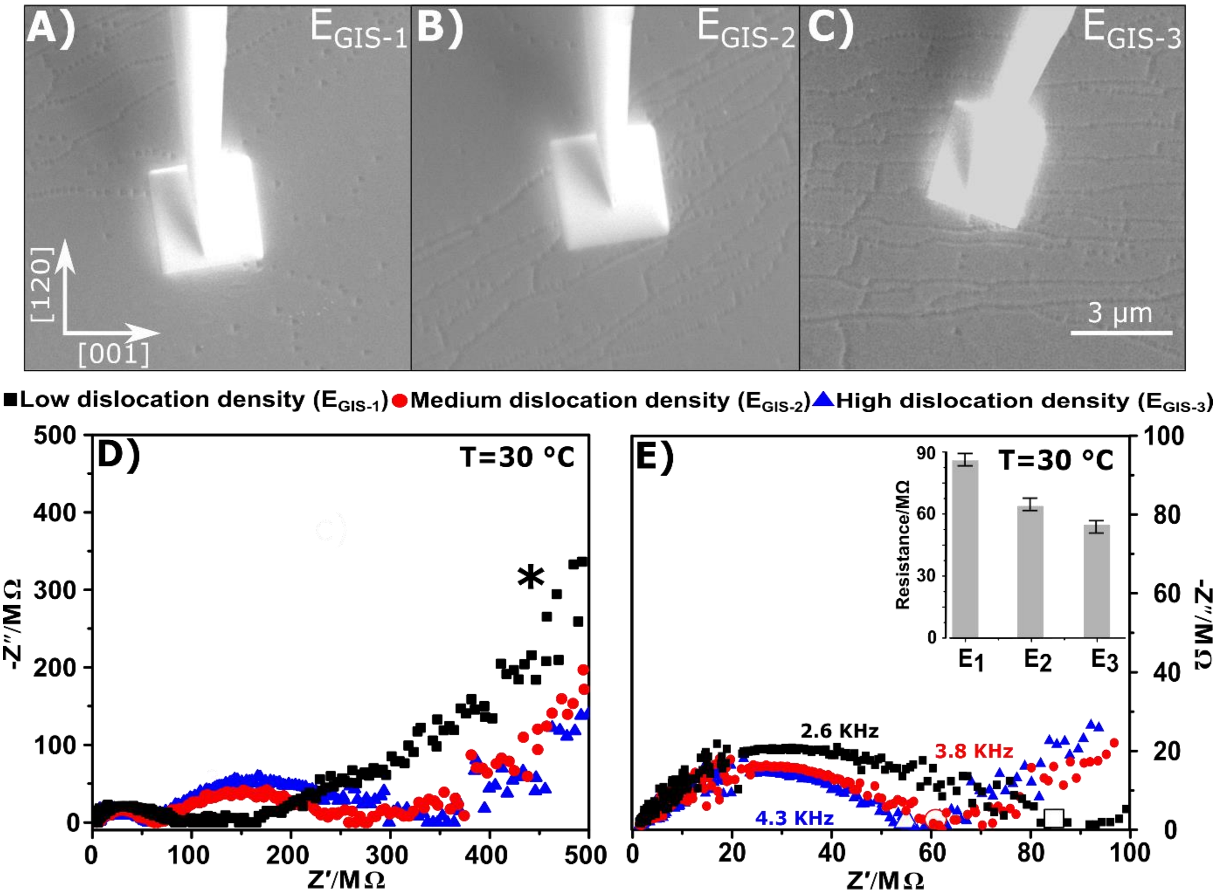

Fig. 5. Microcontact impedance spectroscopy (GIS deposited electrodes). HR-SEM images of electron beam assisted gas injection system (GIS) deposited tungsten microelectrodes onto (**A**) low E_{GIS-1}, (**B**) medium E_{GIS-2}, and (**C**) high dislocation density areas E_{GIS-3}. The area of microelectrodes is 3 × 3 μm^2 while tungsten needles with a tip-diameter of 100 nm are used to probe these electrodes. (**D**) Nyquist plots of impedance measured at room temperature in the frequency range of 100 Hz to 200 kHz. For bundle-like configurations (E_{GIS-2}/ E_{GIS-3}), two contributions are observed. (**E**) Nyquist plots of the same measurement focused here in the range of 2 kHz to 200 kHz. AC frequency values are highlighted at the minima of the respective semicircles, showing the existence of bulk response at lower frequencies (for E_{GIS-1}) and dislocation response (for E_{GIS-2} and E_{GIS-3}) at higher frequencies. Corresponding resistance values are presented in the histogram.

Fig. 5D illustrates Nyquist plots for GIS deposited microcontact measurements for low (E_{GIS-1}), medium (E_{GIS-2}), and high dislocation density (E_{GIS-3}) areas. For bundle-like configurations, i.e., medium (E_{GIS-2}) and high (E_{GIS-3}), two contributions can be observed in Fig. 5D as for the measurements presented in Fig. 4. The second response for E_{GIS-1} simply seems to evolve at much lower frequencies out of the measurement range (marked as *). However, it becomes clear that there is a separation of electrical responses for E_{GIS-1} as well. Multiple impedance spectra are recorded to check for the reproducibility of the results. There is a difference in the resistance of the first response depending on the number of dislocations in the respective regions. This becomes clear in Fig. 5E, in which the data range is limited from 2 kHz to 200 kHz. Corresponding resistance values are evaluated for these measurements and presented in the form of a histogram in the inset, which followed at least a similar trend as the measurement of the *PVD* sputtered microelectrodes. However, while the resistance changes by orders of magnitude for the large microelectrodes, the small GIS electrode measurements reveal changes by only a few percent.

2.3. Finite Element Method (FEM) calculations:

To elucidate the differences between the two measurement approaches and to attribute the electrical responses to physical processes, the data can be compared to the generated exemplary impedance plot from the FEM calculations in Fig. 6.

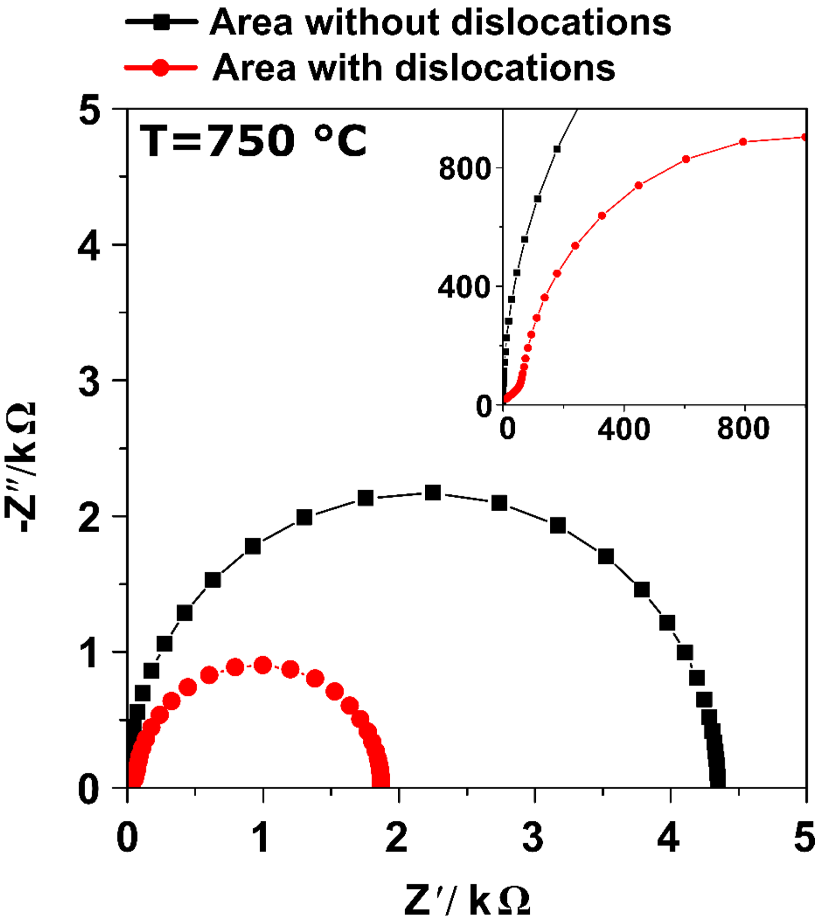

Fig. 6. Exemplary FEM calculations. Nyquist plots of impedance from simulations for areas with and without dislocations. Configuration from Fig. 1 (see Materials and Methods section), i.e., with and without dislocations bundles at T=750 °C.

It can be noted that a high conductive response evolves at high frequency when a dislocation-rich area is present. Therefore, the response can be attributed to the low dislocation resistance. The large resistive response belongs to the gap between dislocation bundles (FEM calculation components shown in Fig. 1/see Materials and Methods section). It is expected that the gap resistance is smaller than that of the bulk. Depending on how large the electrodes are and how many dislocations contribute to the overall response, the high-frequency semicircle can change its shape. For example, the observed changes in resistance of the first dislocation response are not orders of magnitude for the GIS deposited samples (Fig. 5E). Additionally, the measured resistance is more significant, which does not change, taking the microelectrode dimensions into account (comparison of resistivity presented in Fig. S3). The smaller the microelectrodes are, the fewer dislocation arrays (from a bundle) get captured. We estimated the dislocation affected region in previous work to have a diameter of about ≈60 nm (*32*). Given the number of dislocation etch-pits and the area of the microelectrode, the ratio of the area influenced by dislocations in the microelectrode measurements can be rationalized. For example, in the bundled situation for PVD microelectrode (E_{PVD-2}), there are 2800 (± 50) dislocations that cover 3.2% of the electrode area (we define this as area fraction). Similarly, for E_{PVD-3} with 4000 (± 50) dislocations, the area fraction was calculated to be 4.5%. Thus, there is an increase of area fraction by a factor of 1.4 comparing E_{PVD-2} to E_{PVD-3}. This ultimately results in an increase of local conductivity by a factor of 4. For E_{PVD-1}, however, only an area fraction of 0.04% could be determined with 40 dislocations present. This means a much more significant change in area fraction (by a factor of 80) from E_{PVD-1} to E_{PVD-2} leads to an increase in local conductivity by a factor of 125 due to this higher ratio. We also note that a higher area fraction correlates with higher conductivity but also understand that this trend is not necessarily linear.

In contrast, for the GIS-deposited microelectrode (E_{GIS-2}), merely 40 (±5) dislocations were captured. This gives an area fraction of 1.6%. There is a difference in area fraction by a factor of 4 compared to E_{GIS-1} (area fraction 0.4%) and increases local conductivity by a factor of 1.3. When the area fraction increases further by 1.6, conductivity becomes higher by a factor of 1.2 (comparing E_{GIS-2} to E_{GIS-3}). Certainly, the numbers can only illustrate the general trend as the affected area is estimated after all, and the degree of space charge overlap cannot be taken into account. Nevertheless, the comparison well explains the deviations of the results from the different microelectrode sizes and supports our present interpretation of the data.

Interestingly, in the results from GIS deposited microelectrodes for low dislocation density area (E_{GIS-1}) in Figs. 5D-E, a dislocation-related response can also be observed. This means that the influence of dislocations on the electrical properties does not vanish completely. However, it may not be resolved, as can be seen from the data for E_{PVD-1} (Fig. 4C), similar to the bulk measurements at high temperatures (*32*). A comparison of the real part of simulated impedance data from full electrode and microelectrode measurements is given in Fig. S2 (in the supplemental). There, it can be observed that the dislocation resistance and the gap response for the full electrode measurement decrease. Thus, the dislocation response becomes more dominant for microelectrode measurements with decreasing electrode size.

2.4. Temperature-dependent conductivity

temperature-dependent microcontact impedance spectroscopy measurements are performed with the setup illustrated in Fig. 4A. Admittance (Y) data pertaining to each electrode is extracted. Fig. 7A depicts the Arrhenius plots and activation energies (E_a) in the temperature range of 30 °C to 100 °C. Interestingly, the huge difference in electrical conductivity between low dislocation density areas and areas with dislocation bundles is found to be temperature independent. There is an increase by orders of magnitude in the electrical conductivity when measuring dislocation bundles compared to the recovered (low dislocation density) region. In addition, the higher the dislocation density, the more prominent is the increase in conductivity. Note here that low dislocation density areas (E_{PVD-1}) exhibit temperature-independent conductivity as well. In this case, only the conductivity attributed to the bulk can be determined. This is possible when extrinsic impurity dopants from the single crystal growth contribute to the bulk conductivity at low temperatures. Furthermore, the frozen changes in defect chemistry, to which rutile is very sensitive, may contribute (*36*). At higher temperatures, as observed in the previous work, the activation energy changes to a higher value (e.g., 0.75 eV) since thermal activation of charge carrier formation sets in (*32*). Therefore, this is seen as a likely scenario.

Furthermore, the gap response (measured at low frequency in Fig. 4B) for medium and high dislocation density areas (E_{PVD-2} and E_{PVD-3}) is also plotted in Fig. 7A. Experimental data follows a similar trend compared to the FEM calculated data, i.e., gap response admittance is shifted to higher values with the activation energies still hinting towards extrinsic electronic conductivity (*36*). However, we observe that the gap response admittance of $E_{\text{PVD-2}}$ is higher than the one from $E_{\text{PVD-3}}$. It may be the case for $E_{\text{PVD-2}}$ that dislocation streaks going into the sample are different from those in $E_{\text{PVD-3}}$. The gap response is not necessarily correlated to the density of the bundles at the surface. Therefore, a higher gap response for $E_{\text{PVD-3}}$ compared to $E_{\text{PVD-2}}$ is certainly possible, and further details will depend on the exact arrangement of the dislocations, which is unfeasible to capture experimentally. Consequently, the trends observed are in excellent agreement with our hypothesis and FEM calculations.

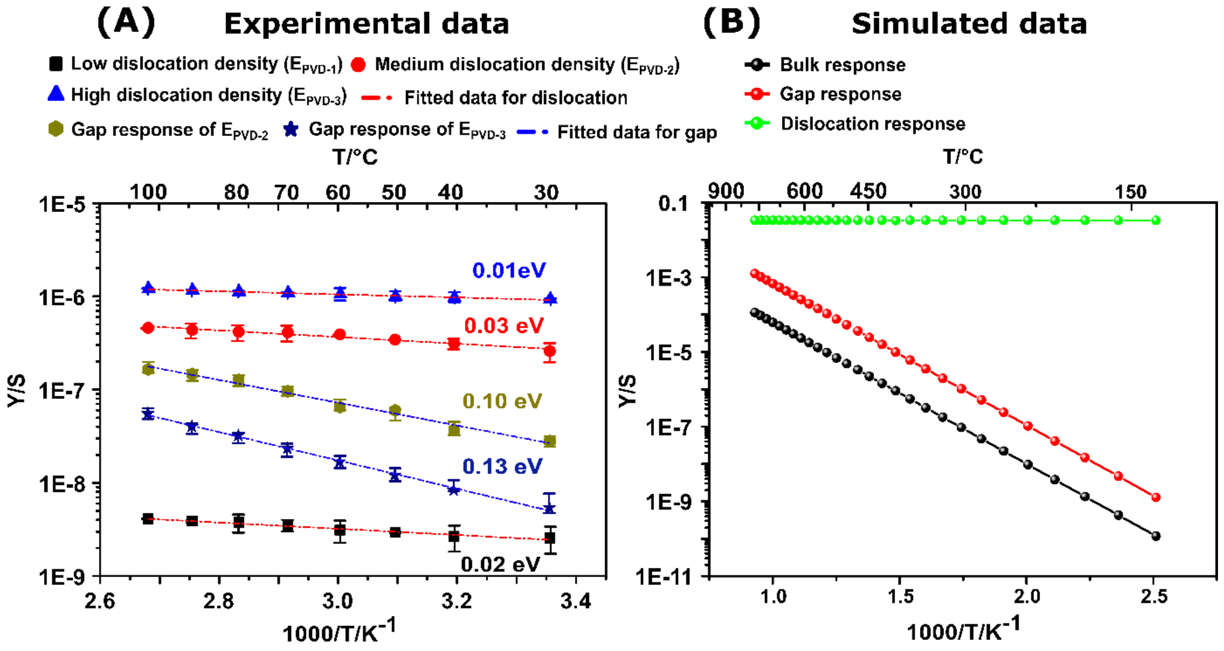

Fig. 7. Experimental and simulated temperature-dependent admittance. (**A**) Arrhenius plots of admittance for low ($E_{\text{PVD-1}}$), medium ($E_{\text{PVD-2}}$), and high dislocation density ($E_{\text{PVD-3}}$) areas, as well as the gap response of EPVD-2 and EPVD-3, measured in the range of 30 °C to 100 °C along with respective activation energies ($E_{a.}$). The standard deviation for each measurement is evaluated, and error bars are presented. (**B**) Arrhenius plots of admittance for pristine bulk, gap, and the dislocation response evaluated via FEM in the temperature range of 125 °C to 800 °C. The gap response shows the same temperature dependence as the bulk. For the FEM calculations, no extrinsic dopant response is taken into account at low temperatures.

At temperatures above 500 °C and with bulk electrodes, temperature-dependent measurements revealed high activation energy and just a shift in conductivity but no change in the respective activation energy (*32*). The difference to the present results can be further rationalized with the help of the FEM simulations taking a temperature dependence into account. Fig. 7B illustrates results from the evaluation of the simulated impedance data. The lowest conductivity results from the simulation without dislocations (bulk). Two responses can be rationalized for the simulations with dislocations: one belongs to the temperature-independent dislocation properties and the other to the gap response. The gap response follows a similar trend in conductivity, likewise the overall bulk, as reported in Ref. (*32*). But here, the admittance (*Y*) shifted towards higher values as the geometry of bulk and gap are different. Therefore, its contribution to the temperature-dependent admittance is shifted to higher values. However, the FEM calculation depicted in Fig. 7B does not include an extrinsic response for the bulk/gap properties at low temperatures, as is observed in Fig. 7A. Nevertheless, the hypothesis that the impact of dislocations results from a temperature-independent space charge conductivity is excellently supported by the FEM data in comparison to the experimental data in Fig. 7A.

With the presented evaluation of the microelectrode measurements, it could be validated that dislocations can act as highly conductive pathways in rutile. Here, we show that these bundles or arranged mesoscopic dislocation structures induce several orders of magnitude higher electrical conductivity on a local scale. The presented physical interpretation rationalizes the electrical results. Introducing dislocations essentially causes a doping effect, leading to new strategies of modifying functional properties of ceramics apart from chemical doping. Rutile's low electronic conductivity is one of the open challenges to solve for potential application, such as electrode material in solid-state batteries (*37*). To address this, rutile property engineering *via* conventional chemical doping (*37-40*) and composite processing approaches (*41, 42*) are usually considered. Dislocation-enhanced, highly stable, and temperature insensitive electronic conductivity could potentially increase electronic and ion transport for modern solid-state batteries. Furthermore, it will certainly be of great interest how dislocations modify photoelectric properties. It could already be shown for ZnO to modify light absorption significantly (*43*). Therefore, new pathways for the use of TiO_2 in photoelectric applications could be developed.

2.5. Conclusion

In summary, we elucidated the dislocation-enhanced, highly stable electronic conductivity in TiO_2 by using microcontact impedance spectroscopy and supplemented with FEM calculations. An arranged mesoscopic dislocation structure induces several orders of magnitude higher electrical conductivity on a local scale compared to the single crystal bulk. With the established model, the complex individual components involved in the conduction process, i.e., the dislocations and the response from the gap between dislocation bundles, which have bulk properties, are elaborated. Thus, the concept of changing functional properties in ceramics by introducing dislocations appears promising.

3. Materials and Methods

3.1. Experimental design/sample preparation

Rutile single crystals with 99.99% purity, grown *via* Verneuil-flame fusion technique (Alineason Materials Technology GmbH, Frankfurt am Main, Germany), were cut along the [010] direction. This particular orientation offers maximum Schmid factor (0.45) under uniaxial compression for the mobile single slip system {011} <011> (see Fig. S1A) (*44*). Fine optical polishing was performed to remove cutting damage from all sides of the crystals, while orientation accuracy of ± 0.5° was assured by Laue measurements (Laue-Camera GmbH, Dietersheim, Germany). Uniaxial compressive deformation was conducted in a load frame (Z010 Zwick/Roell, Ulm, Germany) with an attached furnace (LK/SHC1500-85-150-1-V-

Sonder, HTM Reetz GmbH, Berlin, Germany) at 1050 °C (under ambient conditions) with a constant strain rate ($\dot{\varepsilon}$) of 2×10^{-4} s^{-1}. Crack-free samples with a plastic strain of 5% were fabricated, as depicted in the true stress-strain diagram (Figs. S1B-C). Specimens of 1 mm thickness with (120) plane orientation were cut from the deformed single crystals (Fig. 2) *via* benchtop diamond wire saw (Wire Saw Solutions Group LLC, PA, USA). This systematic cutting enables electrical measurements along the dislocation lines (schematically shown in Fig. 2). Both sides of the specimens were then finished by mechanical grinding starting with abrasive SiC sandpapers (ATM Qness GmbH, Mammelzen, Germany) of P1200, P2500 (5 min each) followed by automated polishing (Phoenix 4000, Jean Wirtz GmbH, Düsseldorf, Germany) with 6 µm, 3 µm, 1 µm, and ¼ µm diamond paste (DP-Paste Struers, Germany) coated polishing discs (MD Struers, Germany) at 300 rev min^{-1} (15 min each). Residual damage from polishing the surface was removed with extremely gentle vibrational polishing (for 12 h) in 40 ml solution of water and 0.04 µm colloidal silica (OP-S, Struers A/S, Ballerup, Denmark) with an optimized ratio of 8:1.

3.2. Visualization of dislocations

The mesoscopic dislocation structure was visualized on (120) planes *via* chemical etching (etching patterns illustrated in Fig. 2). With this technique, small *etch-pits* form onto the sample surface where the etching solution preferentially attacks the dislocation intercepting the surface (*45*). In our case, vibro-polished rutile specimens with (120) planes were immersed in 70% KOH buffer (Emplura, Merck KGaA, Darmstadt, Germany) at 370 °C for 4.5 min, followed by neutralization in 1M H_2SO_4 for 1 min.

3.3. Annealing treatment

After cleaning the samples, thermal annealing is carried out at 600 °C for 1 h in a tube furnace with a heating and cooling rate of 3 K/min. This annealing step profoundly impacts the defect chemistry of rutile and the reproducibility of results. It has been established that point defects in rutile have a tendency to coalesce into a lower energy configuration only under very slow cooling; if higher cooling rates are applied, irreproducible defect chemical states can be induced (*46*). Parameters such as annealing temperature, time duration, heating, and cooling rates are optimized in this work. For this purpose, 4 slices of a deformed crystal were annealed up to 600 °C at several but equal heating and cooling rates, e.g., 10 K/min, 7 K/min, 5 K/min, and 3 K/min, respectively. The latter heating/cooling rate was found to provide reproducible electrical data (details in supplemental). Furthermore, note that annealing temperature (600 °C) is well below the recovery temperature (1020 °C), so a change in mesoscopic dislocation structure is not expected.

3.4. High-resolution laser and scanning electron microscopy

Chemically etched and annealed samples were examined under a laser microscope (LEXT; OLS4000- Olympus Corporation, Tokyo, Japan) to identify dislocation-free (recovered) and high dislocation density (bundle-like) regions. Also, quantitative analysis of respective regions was fully rationalized with the help of high-resolution scanning electron microscopy (HR-SEM/XL30FEG, Philips, Amsterdam, Netherlands) before and after the microelectrode deposition.

3.5. Microelectrode deposition

Two different deposition strategies, including physical vapor deposition *(PVD)* and electron beam assisted-gas injection system *(GIS)*, were employed to furnish microcontacts onto the recovered region (low dislocation density) and the dislocation bundles with medium and high dislocation density (further details in the respective section).

3.6. Microcontact impedance spectroscopy

Microcontact impedance spectroscopy (MCIS) is employed to detect and quantify the local electrical response of the mesoscopic dislocation structure. It offers excellent potential to investigate dislocation-free and high dislocation density regions. Only a small volume below the electrode is probed, which provides a good idea of the local electrical conductivity of dislocations in terms of spreading resistance (*34, 47*). MCIS measurements were conducted *via* microprobe setup (MPS150, Cascade Microtech GmbH, Aschheim, Germany) equipped with a Novocontrol Alpha-A impedance analyzer (Novocontrol Technologies GmbH & Co. KG, Montabaur, Germany) in the frequency range between 3MHz and 1 Hz with an amplitude of 1V. Two tungsten needles (PTT-12-25, Cascade Microtech GmbH, Aschheim, Germany) with a tip diameter of 1.2 µm were employed to probe microcontacts. Measurements in the temperature range of 30 °C -100 °C were performed with a small heater (Linkam Scientific Instruments, Tadham, UK) encapsulated in alumina concealment. Each temperature-dependent data point is measured after holding for 30 min to ensure stable impedance spectra (schematic of MCIS setup is presented in Fig. 4A).

3.7. Finite Element Method (FEM) calculations

FEM calculations were conducted to support the evaluation of the electrical results simulating the hypothesized impact of dislocations (COMSOL, Inc., Massachusetts, USA). An electrical current (ec) calculation in the frequency domain was set up. A 2D geometry was employed defining a sample of 1 cm width and 0.5 cm height (Fig. 1/see Materials and Methods section) using a triangular mesh. The bulk conductivity was varied in a parametric study according to $\sigma = \sigma_0 \cdot exp\left(\frac{E_a}{k_b T}\right)$, with $\sigma_0 = 0.4$ S/m and the activation energy $E_a = 0.75$ eV (*32*). The parameters k_b and T have their established meaning Boltzmann constant and temperature, respectively. This emulates the observed TiO_2 bulk behavior well. Bundles of dislocations extend from the surface into the bulk at an angle of 45° to account for the slip system not being 90° with the cutting face. The bundles are assumed to consist of dislocations with overlapping space charges, and thus it is unlikely that conductivity variation occurs within them ($\sigma_{disloc} = 0.01$ S/m). Furthermore, the space charge conductivity is not expected to be temperature-dependent. The mesh is refined in these regions. In the previous work, it could be illustrated that roughly 1.9% of the whole crystal surface is covered with dislocations (*32*). Therefore, the bundles were chosen to spread accordingly along this area. A microelectrode of 20 μm was put on top of a dislocation bundle and defined as terminal. The full opposite surface was defined as the counter electrode. With these boundary conditions, the frequency and temperature-dependent electrical response were calculated to be compared to the measured impedance data.

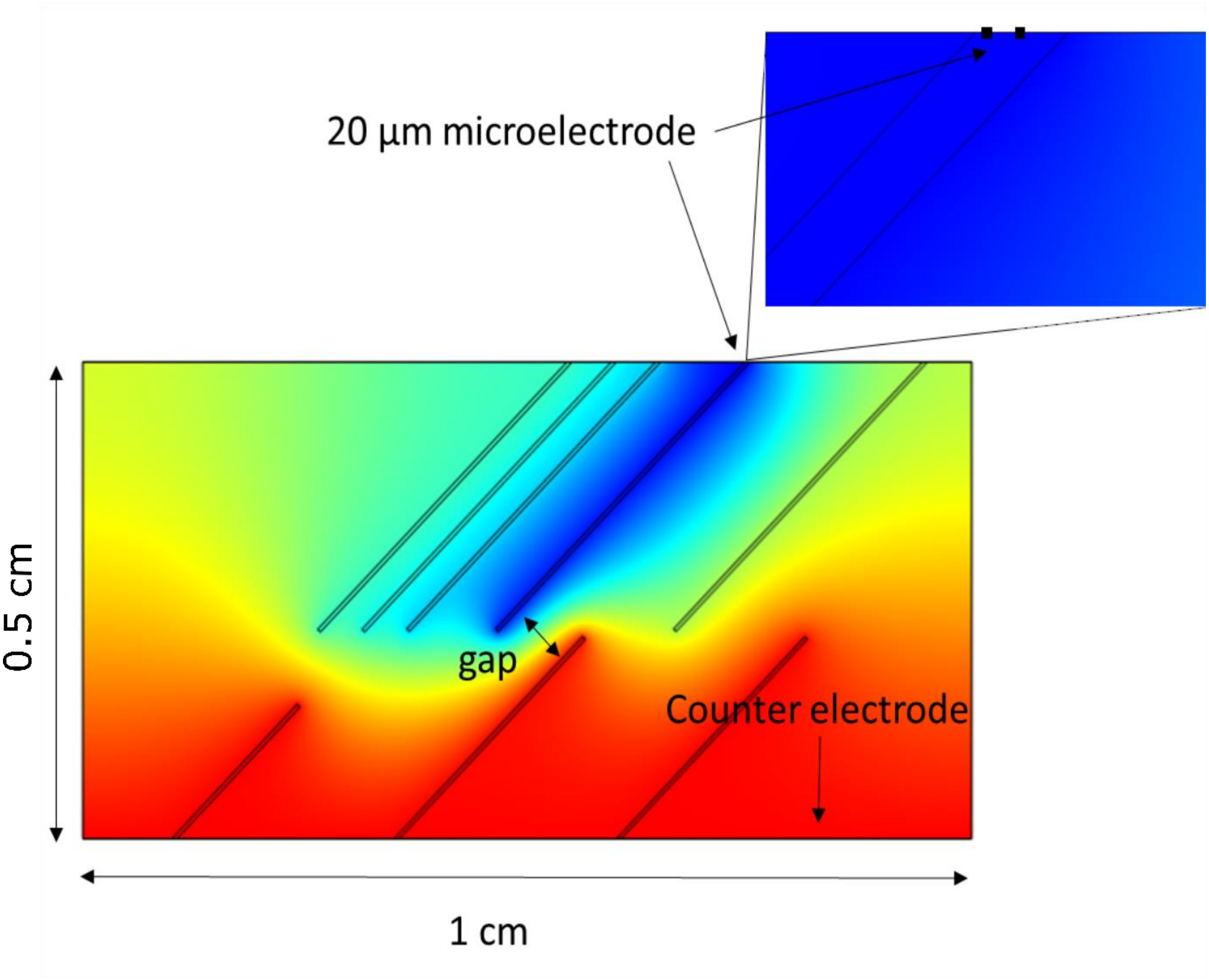

Fig. 1. Finite Element Method (FEM) calculations. Distribution of potential for a microelectrode deposited on a dislocation-rich region simulated by FEM (25 °C, 1 kHz). Dislocation bundles displayed in black are arranged in an arbitrary example configuration.

4. References and notes

1. K. Szot, C. Rodenbücher, G. Bihlmayer, W. Speier, R. Ishikawa, N. Shibata, Y. Ikuhara, Influence of dislocations in transition metal oxides on selected physical and chemical properties. *Crystals* **8**, 241 (2018).
2. J. Amodeo, S. Merkel, C. Tromas, P. Carrez, S. Korte-Kerzel, P. Cordier, J. Chevalier, Dislocations and plastic deformation in MgO crystals: a review. *Crystals* **8**, 240 (2018).
3. R. Whitworth, Charged dislocations in ionic crystals. *Adv. Phys.* **24**, 203-304 (1975).
4. P. M. Anderson, J. P. Hirth, J. Lothe, *Theory of dislocations* (Cambridge University Press, 2017).
5. J. Hirth, A brief history of dislocation theory. *Metallurgical Transactions A* **16**, 2085-2090 (1985).
6. J. Gilman, W. Johnston, Dislocations in lithium fluoride crystals. *Solid state physics* **13**, 147-222 (1962).
7. A. Nakamura, K. Matsunaga, J. Tohma, T. Yamamoto, Y. Ikuhara, Conducting nanowires in insulating ceramics. *Nat. Mater.* **2**, 453-456 (2003).

8. K. Otsuka, K. Matsunaga, A. Nakamura, S. Ii, A. Kuwabara, T. Yamamoto, Y. Ikuhara, Effects of dislocations on the oxygen ionic conduction in yttria stabilized zirconia. *Materials transactions* **45**, 2042-2047 (2004).
9. K. Otsuka, A. Kuwabara, A. Nakamura, T. Yamamoto, K. Matsunaga, Y. Ikuhara, Dislocation-enhanced ionic conductivity of yttria-stabilized zirconia. *Appl. Phys. Lett.* **82**, 877-879 (2003).
10. S. I. Kim, K. H. Lee, H. A. Mun, H. S. Kim, S. W. Hwang, J. W. Roh, D. J. Yang, W. H. Shin, X. S. Li, Y. H. Lee, Dense dislocation arrays embedded in grain boundaries for high-performance bulk thermoelectrics. *Science* **348**, 109-114 (2015).
11. R. Deng, X. Su, Z. Zheng, W. Liu, Y. Yan, Q. Zhang, V. P. Dravid, C. Uher, M. G. Kanatzidis, X. Tang, Thermal conductivity in $Bi_{0.5}Sb_{1.5}Te_{3+x}$ and the role of dense dislocation arrays at grain boundaries. *Science advances* **4**, eaar5606 (2018).
12. M. Johanning, L. Porz, J. Dong, A. Nakamura, J.-F. Li, J. Rödel, Influence of dislocations on thermal conductivity of strontium titanate. *Appl. Phys. Lett.* **117**, 021902 (2020).
13. P. Ren, M. Höfling, J. Koruza, S. Lauterbach, X. Jiang, T. Frömling, D. K. Khatua, C. Dietz, L. Porz, R. Ranjan, High temperature creep-mediated functionality in polycrystalline barium titanate. *J. Am. Ceram. Soc.* **103**, 1891-1902 (2020).
14. U. Messerschmidt, *Dislocation dynamics during plastic deformation* (Springer Science & Business Media, 2010).
15. L. Porz, T. Frömling, A. Nakamura, N. Li, R. Maruyama, K. Matsunaga, P. Gao, H. Simons, C. Dietz, M. Rohnke, J. Janek, J. Rödel, Conceptual Framework for Dislocation-Modified Conductivity in Oxide Ceramics Deconvoluting Mesoscopic Structure, Core, and Space Charge Exemplified for $SrTiO_3$. *ACS Nano*, (2020).
16. Y. Oshima, A. Nakamura, K. Matsunaga, Extraordinary plasticity of an inorganic semiconductor in darkness. *Science* **360**, 772-774 (2018).
17. Y. Oshima, A. Nakamura, K. P. D. Lagerlöf, T. Yokoi, K. Matsunaga, Room-temperature creep deformation of cubic ZnS crystals under controlled light conditions. *Acta Materialia* **195**, 690-697 (2020).
18. B. Feng, R. Ishikawa, A. Kumamoto, N. Shibata, Y. Ikuhara, Atomic Scale Origin of Enhanced Ionic Conductivity at Crystal Defects. *Nano letters* **19**, 2162-2168 (2019).
19. R. A. De Souza, J. Fleig, J. Maier, Z. Zhang, W. Sigle, M. Rühle, Electrical resistance of low-angle tilt grain boundaries in acceptor-doped $SrTiO_3$ as a function of misorientation angle. *J. Appl. Phys.* **97**, 053502 (2005).
20. Y. Furushima, A. Nakamura, E. Tochigi, Y. Ikuhara, K. Toyoura, K. Matsunaga, Dislocation structures and electrical conduction properties of low angle tilt grain boundaries in $LiNbO_3$. *J. Appl. Phys.* **120**, 142107 (2016).
21. F. Javaid, E. Bruder, K. Durst, Indentation size effect and dislocation structure evolution in (001) oriented $SrTiO_3$ Berkovich indentations: HR-EBSD and etch-pit analysis. *Acta Materialia* **139**, 1-10 (2017).
22. X. Fang, L. Porz, K. Ding, A. Nakamura, Bridging the Gap between Bulk Compression and Indentation Test on Room-Temperature Plasticity in Oxides: Case Study on $SrTiO_3$. *Crystals* **10**, 933 (2020).
23. L. Jin, X. Guo, C. Jia, TEM study of<110>-type 35.26° dislocations specially induced by polishing of $SrTiO_3$ single crystals. *Ultramicroscopy* **134**, 77-85 (2013).
24. A. Tikhonovsky, M. Bartsch, U. Messerschmidt, Plastic deformation of yttria stabilized cubic zirconia single crystals I. Activation parameters of deformation. *physica status solidi (a)* **201**, 26-45 (2004).
25. S. Taeri, D. Brunner, W. Sigle, M. Rühle, Deformation behaviour of strontium titanate between room temperature and 1800 K under ambient pressure: Dedicated to Professor Dr. Peter Neumann on the occasion of his 65th birthday. *Zeitschrift für Metallkunde* **95**, 433-446 (2004).
26. Y. Ikuhara, Nanowire design by dislocation technology. *Progress in materials science* **54**, 770-791 (2009).
27. W. Johnston, J. Gilman, Dislocation multiplication in lithium fluoride crystals. *J. Appl. Phys.* **31**, 632-643 (1960).

28. P. Gumbsch, S. Taeri-Baghbadrani, D. Brunner, W. Sigle, M. Rühle, Plasticity and an inverse brittle-to-ductile transition in strontium titanate. *Physical Review Letters* **87**, 085505 (2001).
29. E. A. Patterson, M. Major, W. Donner, K. Durst, K. G. Webber, J. Rödel, Temperature-dependent deformation and dislocation density in $SrTiO_3$ (001) single crystals. *J. Am. Ceram. Soc.* **99**, 3411-3420 (2016).
30. K. K. Adepalli, M. Kelsch, R. Merkle, J. Maier, Influence of line defects on the electrical properties of single crystal TiO_2. *Adv. Funct. Mater.* **23**, (2013).
31. K. K. Adepalli, M. Kelsch, R. Merkle, J. Maier, Enhanced ionic conductivity in polycrystalline TiO_2 by "one-dimensional doping". *Phys. Chem. Chem. Phys.* **16**, 4942-4951 (2014).
32. Q. K. Muhammad, L. Porz, A. Nakamura, K. Matsunaga, M. Rohnke, J. Janek, J. Rödel, T. Frömling, Donor and acceptor-like self-doping by mechanically induced dislocations in bulk TiO_2. *Nano Energy*, 105944 (2021).
33. H. Bell, V. Krishnamachari, J. Jones, Recovery of High-Temperature Creep-Resistant Substructure in Rutile. *J. Am. Ceram. Soc.* **55**, 6-10 (1972).
34. J. Fleig, Microelectrodes in solid state ionics. *Solid State Ionics* **161**, 279-289 (2003).
35. J. T. Irvine, D. C. Sinclair, A. R. West, Electroceramics: characterization by impedance spectroscopy. *Adv. Mater.* **2**, 132-138 (1990).
36. T. Bak, J. Nowotny, M. Rekas, C. Sorrell, Defect chemistry and semiconducting properties of titanium dioxide: III. Mobility of electronic charge carriers. *Journal of Physics and Chemistry of Solids* **64**, 1069-1087 (2003).
37. M. Madian, A. Eychmüller, L. Giebeler, Current advances in TiO_2-based nanostructure electrodes for high performance lithium ion batteries. *Batteries* **4**, 7 (2018).
38. M. Fehse, S. Cavaliere, P. Lippens, I. Savych, A. Iadecola, L. Monconduit, D. Jones, J. Roziere, F. Fischer, C. Tessier, Nb-doped TiO_2 nanofibers for lithium ion batteries. *J. Phys. Chem. C* **117**, 13827-13835 (2013).
39. N. A. Kyeremateng, F. Vacandio, M.-T. Sougrati, H. Martinez, J.-C. Jumas, P. Knauth, T. Djenizian, Effect of Sn-doping on the electrochemical behaviour of TiO_2 nanotubes as potential negative electrode materials for 3D Li-ion micro batteries. *Journal of Power Sources* **224**, 269-277 (2013).
40. D. McNulty, E. Carroll, C. O'Dwyer, Rutile TiO_2 Inverse Opal Anodes for Li-Ion Batteries with Long Cycle Life, High-Rate Capability, and High Structural Stability. *Advanced Energy Materials* **7**, 1602291 (2017).
41. N. D. Petkovich, B. E. Wilson, S. G. Rudisill, A. Stein, Titania-Carbon Nanocomposite Anodes for Lithium Ion Batteries, Effects of Confined Growth and Phase Synergism. *ACS Applied Materials & Interfaces* **6**, 18215-18227 (2014).
42. M. Zhen, X. Guo, G. Gao, Z. Zhou, L. Liu, Rutile TiO_2 nanobundles on reduced graphene oxides as anode materials for Li ion batteries. *Chemical Communications* **50**, 11915-11918 (2014).
43. I. Markevich, V. Kushnirenko, L. Borkovska, B. Bulakh, A. Rusavsky, Influence of dislocation decoration with mobile donors on exciton luminescence in ZnO crystals. *physica status solidi c* **4**, 3086-3089 (2007).
44. K. Ashbee, R. Smallman, Stress-strain behavior of titanium dioxide (rutile) single crystals. *J. Am. Ceram. Soc.* **46**, 211-214 (1963).
45. W. Hirthe, J. O. Brittain, Journal of the American Ceramic Society, Dislocations in Rutile as Revealed by the Etch-Pit Technique. **45**, 546-554 (1962).
46. D. M. Smyth, *The defect chemistry of metal oxides* (Oxford University Press, 2000).
47. S. Rodewald, J. Fleig, J. Maier, Microcontact impedance spectroscopy at single grain boundaries in Fe-doped $SrTiO_3$ polycrystals. *J. Am. Ceram. Soc.* **84**, 521-530 (2001).
48. J. Rösler, H. Harders, M. Bäker, *Mechanisches Verhalten der Werkstoffe* (Springer-Verlag, 2012).

Acknowledgments

We are grateful to Prof. Jürgen Rödel (Technical University of Darmstadt) for the helpful discussions.

Funding:

Deutscher Akademischer Austauschdienst (DAAD) Ph.D. fellowship grant number 91669061 (QM)

Deutsche Forschungsgemeinschaft (DFG) grant number 398795637 (LP)

ERC Advanced Grant GB CORRELATE; 787446 GB-CORRELATE (HB and GD)

Author contributions (CRediT):

Conceptualization: QM, LP, TF

Experimental design and data curation: QM, HB

FEM calculations: TF

Writing-original draft: QM, TF

Writing- review & editing: QM, LP, TF, HB, MG, GD

Declaration of Competing Interest:

Authors declare that they have no competing interests.

Data and materials availability:

All data needed to evaluate the conclusions presented in this article is provided in the main text and/or in Supplementary Materials. Additional data related to this research may be requested from the authors.

Figures and Tables: (presented again; as per journal format requirement)

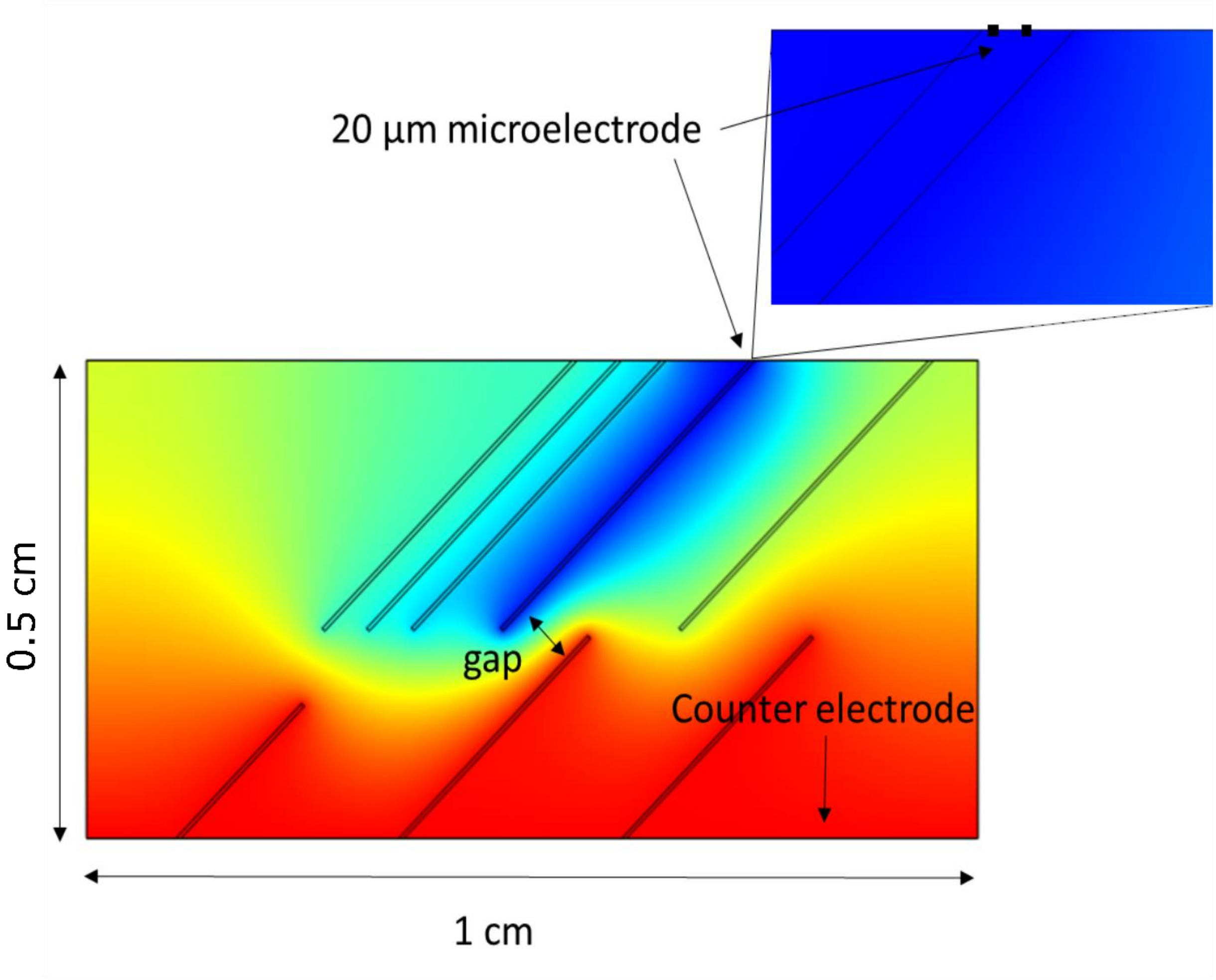

Fig. 2. Finite Element Method (FEM) calculations. Distribution of potential for a microelectrode deposited on a dislocation-rich region simulated by FEM (25 °C, 1 kHz). Dislocation bundles displayed in black are arranged in an arbitrary example configuration.

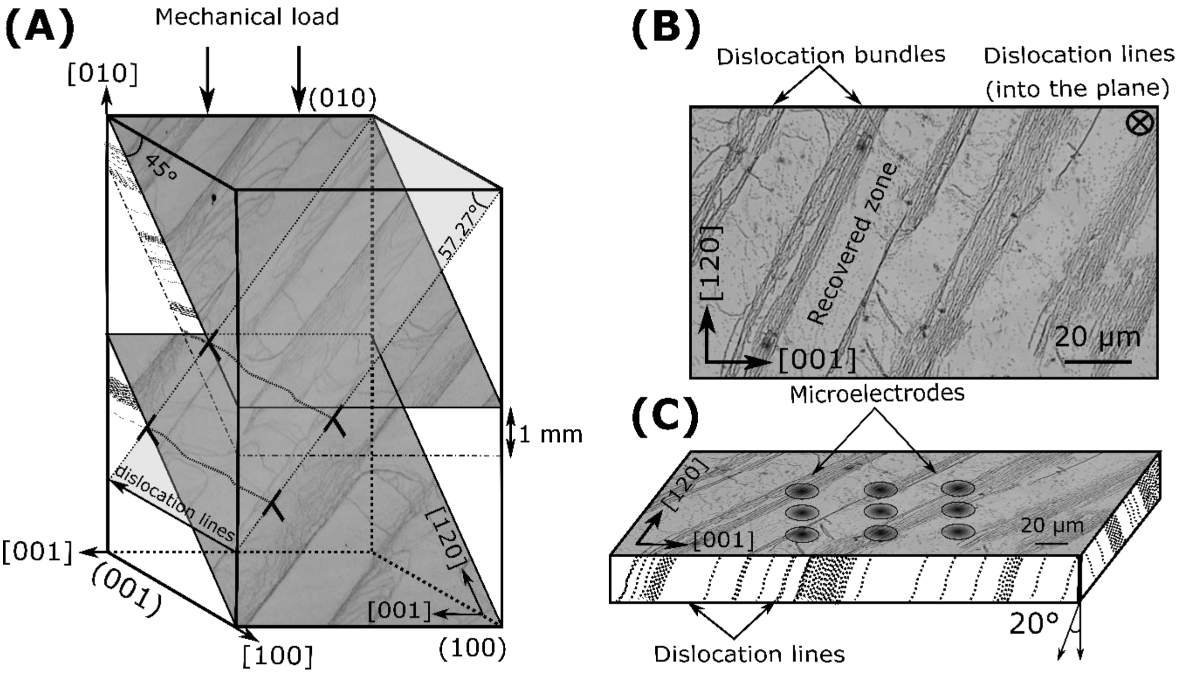

Fig. 2. Conceptualization of experimental design. (**A**) schematic of crystal orientation and loading direction of rutile single crystals (along with activated predominant {011} <011> slip system at an angle of 57.27° with the (010) plane, highlighted in dotted grey (also see Fig. **S1A**). Laser microscope images of chemically etched (120) planes of exactly the same region are presented, recovery behavior can be observed onto the etched planes. Dislocation lines move on the (011) plane in the direction of [100], intersecting (120) plane at an angle, dislocations are visualized as etch-pits onto (120) planes. (**B**) front view of 1 mm thick specimen with etched (120) plane extracted from (**A**), mesoscopic dislocation structure is perceptible at higher magnification while dislocation lines going into the plane (symbol ⊗), recovered zone, and dislocation bundles are optically rationalized. (**C**) schematic of the same specimen in (**B**) with actual micrograph on the top (dislocation lines go through the sample at an angle of ≈ 20°) along with the schematic of targeted microelectrodes onto the dislocation bundles as well as the recovered zone.

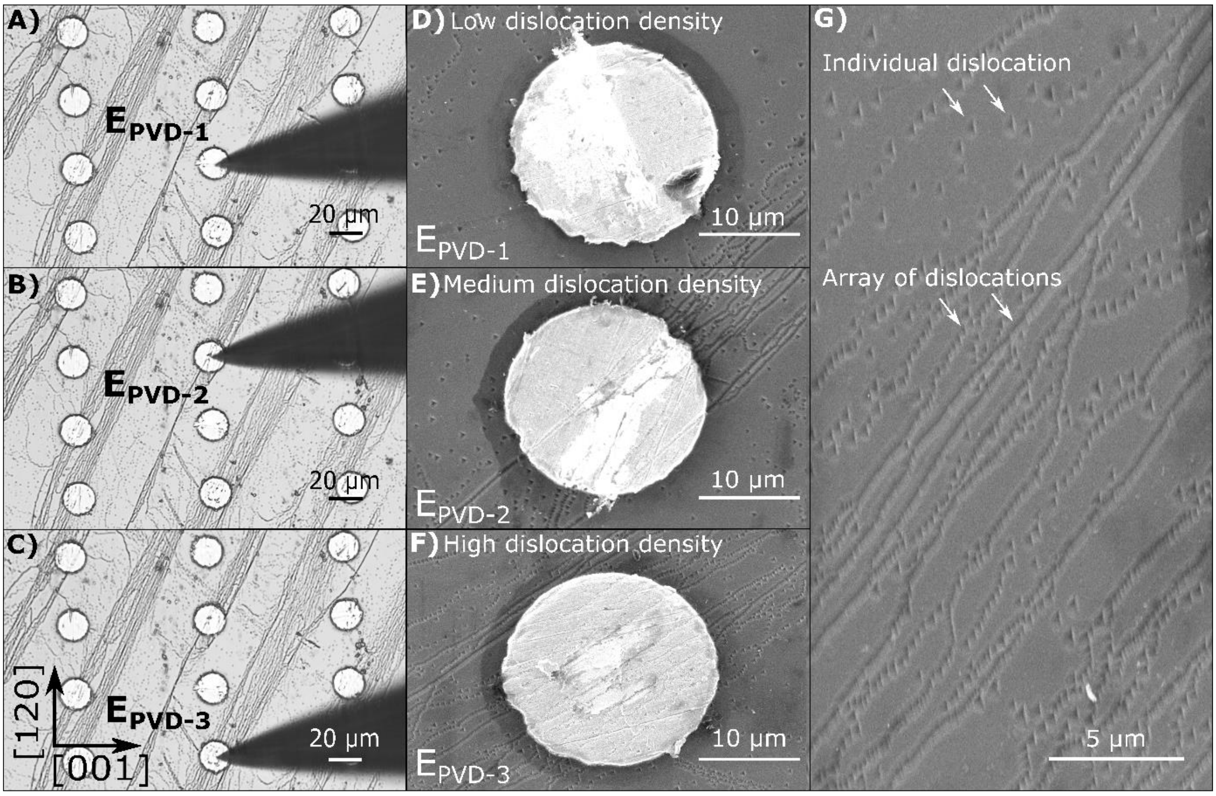

Fig. 3. Arranged mesoscopic dislocation structure and microelectrodes. (**A-C**) Laser microscope images of the specimens with Al-Au microelectrodes of 20 µm diameter. E_{PVD-1}, $E_{PVD-2,}$ and E_{PVD-3} represent recovered zone, bundled regions with medium and high dislocation density, respectively. (**D-F**) Scanning Electron Microscope (SEM) images of microelectrodes furnished in the recovered zone (low dislocation density) E_{PVD-1}, bundled regions with medium (E_{PVD-2}), and high dislocation density (E_{PVD-3}). (**G**) high-resolution SEM image of the same sample before deposition of the microelectrodes depicts etch-pits from the mesoscopic dislocation structure.

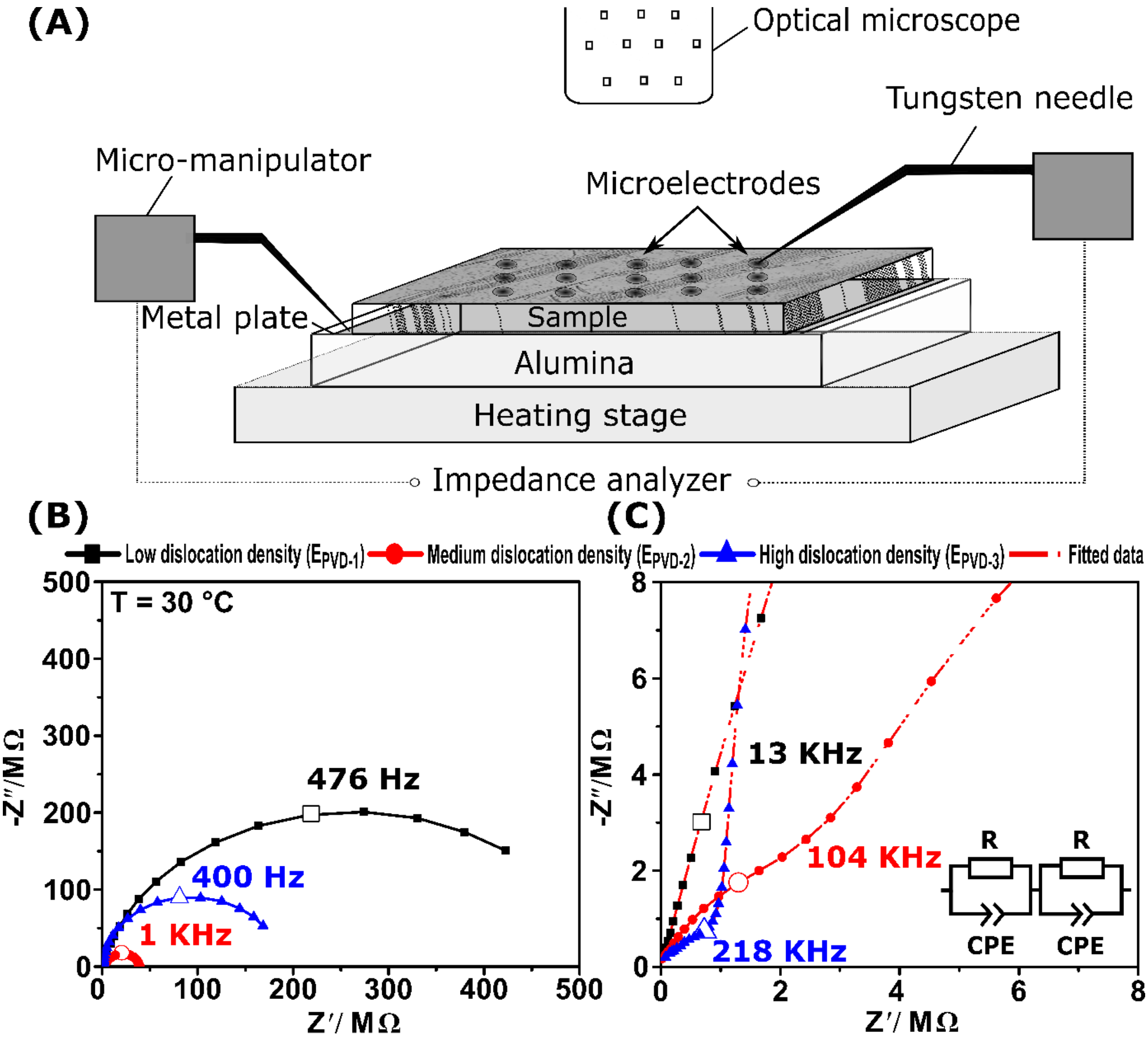

Fig. 4. Microcontact impedance spectroscopy (PVD deposited electrodes). (**A**) Schematic of the microcontact impedance setup depicting heating stage, alumina case, and the sample. The actual micrograph is presented along with the schematic of microelectrodes. Two-probe measurement setup is employed; one tungsten needle is used to probe upper microelectrodes while the other contacts the large metal plate at the bottom electrode. (**B**) Nyquist plots of impedance for selected microelectrodes (at room temperature); onto low (E_{PVD-1}), medium (E_{PVD-2}), and high dislocation density areas (E_{PVD-3}), (AC frequency values are labeled at the capacitance maxima). No Schottky barrier is observed within the measurement frequency range. (**C**) Aside from the bulk response visible for all three electrodes, E_{PVD-2} and E_{PVD-3} show an additional process at high frequencies attributed to the dislocations. Measured data could be fitted using the equivalent circuit presented in the inset.

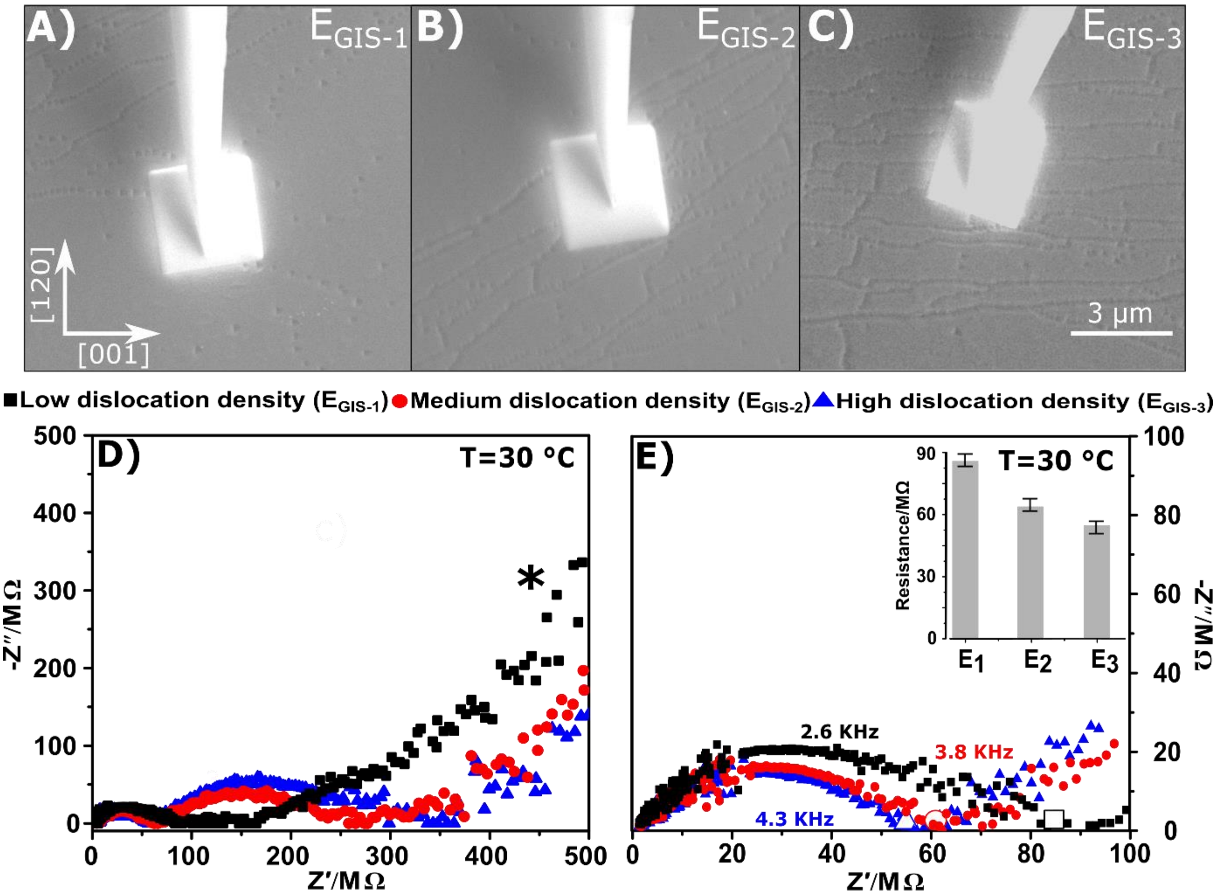

Fig. 5. Microcontact impedance spectroscopy (GIS deposited electrodes). HR-SEM images of electron beam assisted gas injection system (GIS) deposited tungsten microelectrodes onto (**A**) low E_{GIS-1}, (**B**) medium E_{GIS-2}, and (**C**) high dislocation density areas E_{GIS-3}. The area of microelectrodes is 3 × 3 μm^2 while tungsten needles with a tip-diameter of 100 nm are used to probe these electrodes. (**D**) Nyquist plots of impedance measured at room temperature in the frequency range of 100 Hz to 200 kHz. For bundle-like configurations (E_{GIS-2}/ E_{GIS-3}), two contributions are observed. (**E**) Nyquist plots of the same measurement focused here in the range of 2 kHz to 200 kHz. AC frequency values are highlighted at the minima of the respective semicircles, showing the existence of bulk response at lower frequencies (for E_{GIS-1}) and dislocation response (for E_{GIS-2} and E_{GIS-3}) at higher frequencies. Corresponding resistance values are presented in the histogram.

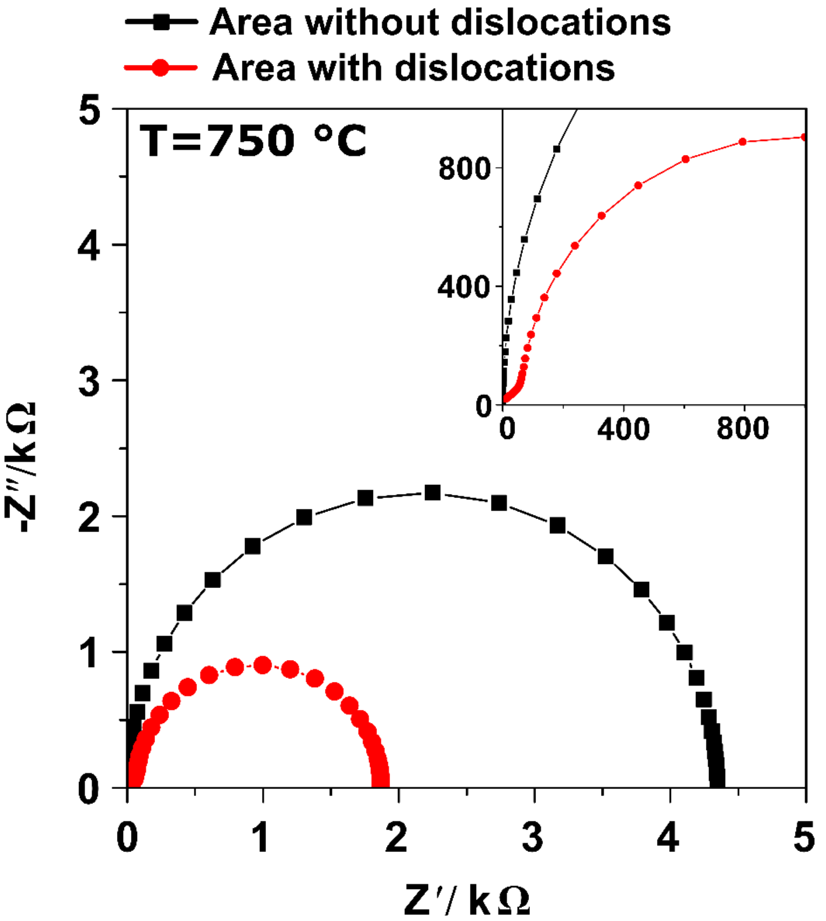

Fig. 6. Exemplary FEM calculations. Nyquist plots of impedance from simulations for areas with and without dislocations. Configuration from Fig. 1 (see Materials and Methods section), i.e., with and without dislocations bundles at T=750 °C.

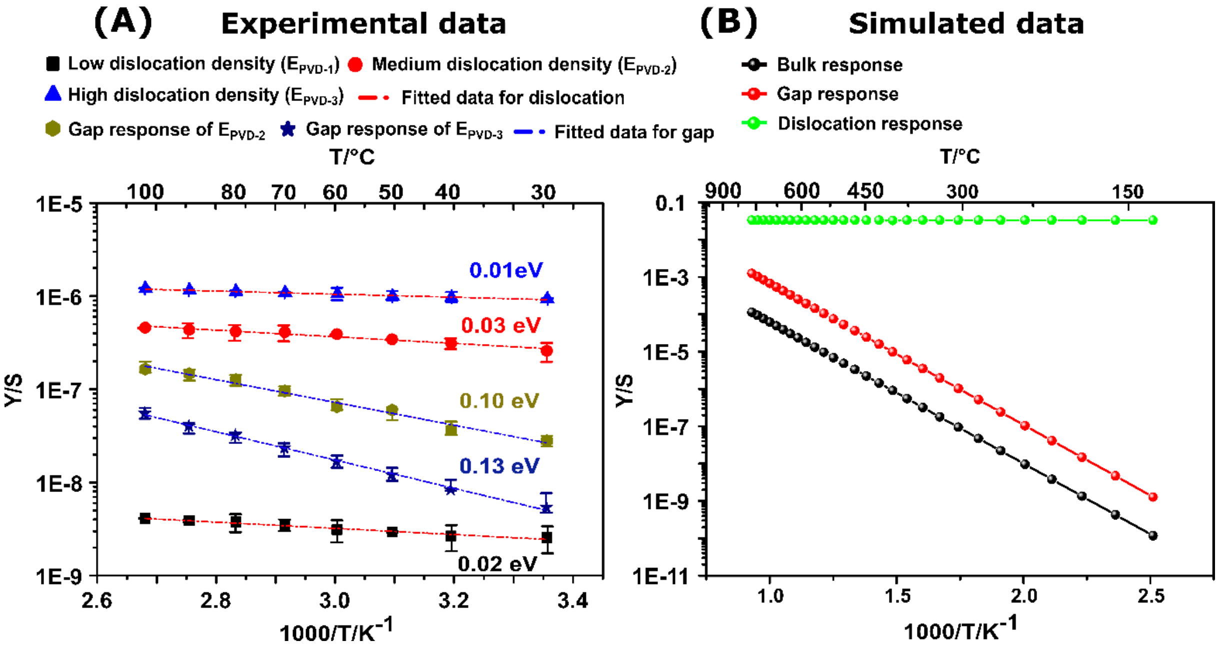

Fig. 7. Experimental and simulated temperature-dependent admittance. (**A**) Arrhenius plots of admittance for low (E_{PVD-1}), medium (E_{PVD-2}), and high dislocation density (E_{PVD-3}) areas, as well as the gap response of E_{PVD-2} and E_{PVD-3}, measured in the range of 30 °C to 100 °C along with respective activation energies ($E_{a.}$). The standard deviation for each measurement is evaluated, and error bars are presented. (**B**) Arrhenius plots of admittance for pristine bulk, gap, and the dislocation response evaluated via FEM in the temperature range of 125 °C to 800 °C. The gap response shows the same temperature dependence as the bulk. For the FEM calculations, no extrinsic dopant response is taken into account at low temperatures.

Supplementary Materials:

Fig. S1A features a schematic illustration of mechanics parameters considered during uniaxial deformation. This includes compression axis ($\overrightarrow{F_c}$) parallel to (010) plane, active slip plane (A), while Burgers vector ($\vec{b}$) (pointing towards the direction of slip) and a perpendicular to the slip plane ($\vec{n}$). To elucidate the Schmid factor pertaining to deformation along [010] direction angles such as θ (between $\overrightarrow{F_c}$ and $\vec{n}$) and λ (between $\overrightarrow{F_c}$ and $\vec{b}$) are presented. The critical resolved shear stress for {011} <011> slip system is as follows:

$$\tau = \sigma \cos\lambda \,.\, \cos\theta$$

Where σ is the yield strength, λ is the angle between <011> slip direction and the compression axis, while θ is the angle between normal to the {011} slip plane and the axis of compression. These two angles (λ and θ) are found to be 32.73° and 57.27°, respectively, whereas the Schmid factor ($\cos\lambda \,.\, \cos\theta$) was evaluated to be 0.45 (*44*).

Fig. S1B shows the true stress-strain curve experimentally obtained by uniaxial deformation of [c-010] oriented rutile single crystals at 1050 °C, a maximum of 5% plastic strain is achieved near to 80 MPa stress level. The transition stress, from linear (elastic shown as E) to non-linear (plastic shown as P) behavior (also termed as yield strength /σ_{ys}), is found to be ≈ 10 MPa, as shown in Fig. S1B. Since it is hard to determine at which stress this transition takes place, Hookean behavior is measured and yield strength $\sigma_{ys_{0.2\%}}$ of 16 MPa is considered as depicted in Fig. S1C. (*48*). It can be seen that compressive strain is increased with the rise in flow stress. Although rutile lattice is rotated to obtain maximum plastic strain yet strain hardening is observed, which is well supported by the literature (*14*, *44*).

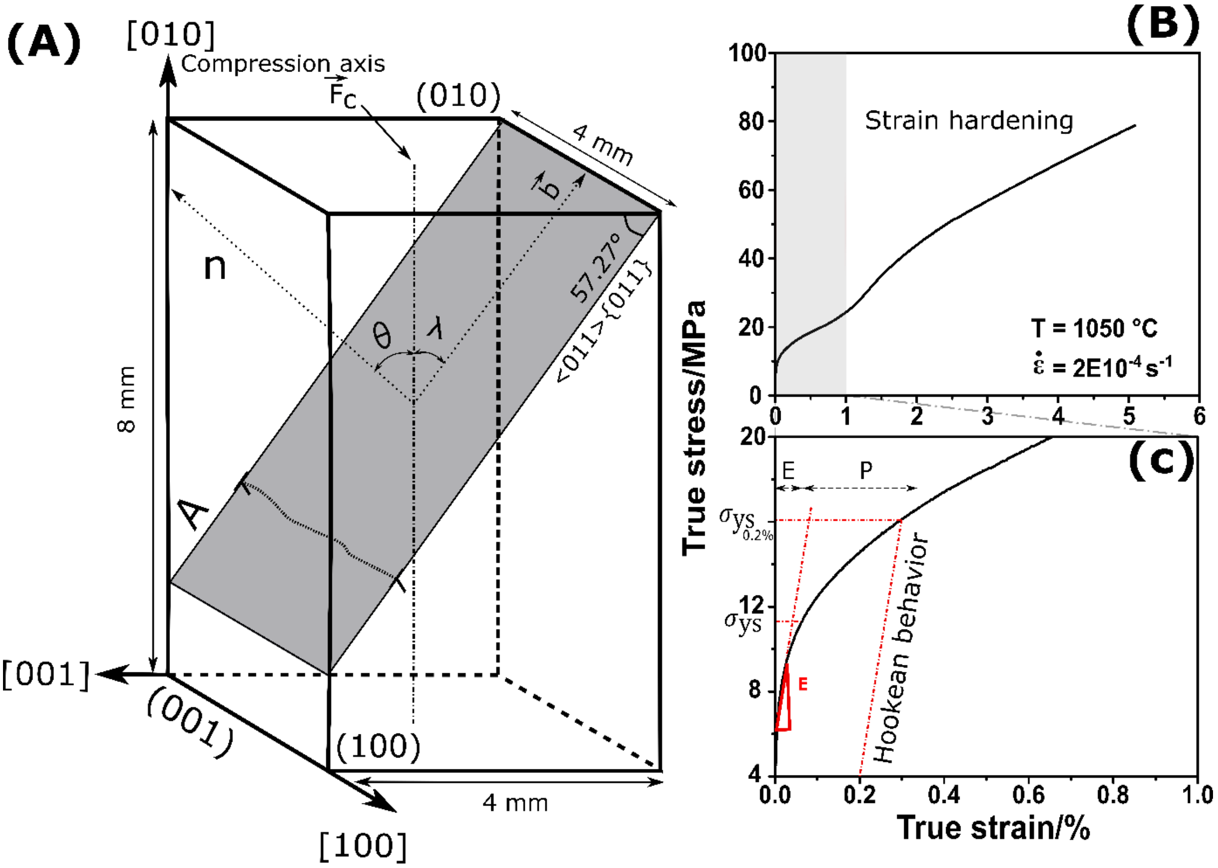

Fig. S1. Mechanics parameters for uniaxial deformation. (**A**) schematic of the geometry, orientation, and primary slip system of rutile single crystals used for mechanical deformation. Compression axis ($\vec{F_c}$), representative glide plane (A), Burgers vector ($\vec{b}$) and normal to the glide plane ($\vec{n}$) are labeled. The preferred glide plane is shaded in grey; dislocations can move onto this glide plane in the direction of the line vector [100], exemplified as a dotted line. Active angles such as θ (between $\vec{F_c}$ and $\vec{n}$) and λ (between $\vec{F_c}$ and $\vec{b}$) are presented to schematically illustrate Schmid factor evaluation. (**B**) obtained true stress-strain curve when rutile samples deformed at 1050 °C, ample strain hardening is observed until 5% plastic strain. (**C**) shaded zone of (**B**) where the elastic and plastic zone are discernable, 0.2% Hookean behavior is excluded to evaluate yield strength ($\sigma_{ys_{0.2\%}}$).

Photolithography for *PVD* electrodes:

Photolithography was employed to fabricate microelectrode patterns on the dislocation bundles and dislocation-free regions (schematically presented in Fig. 2C). Scratchless and dirt-free specimens were spin-coated with negative photoresist polymer (ma-N 1410; micro resist technology GmbH, Berlin, Germany), spinning at 3000 rpm resulted in a 1 µm thick layer of photoresist. To remove the volatile solvent, specimens were heated on a hot plate at 90 °C for 2 min followed by UV-light exposure in a mask aligner (SÜSS MicroTec; MA 56 M, Garching, Germany) for an optimized interval of 40 seconds. Specimens were then dipped into photoresist developer (micro resist technology GmbH; Berlin, Germany) for 80 seconds; this resulted in degradation of unexposed regions and left behind 20 µm diameter imprints. Later, the physical vapor deposition *(PVD)* technique (Quorum Technologies Ltd; Q300 T D Plus) was used to sputter aluminum-gold (Al-Au) layers to furbish microelectrodes at current intensity and time of 150 mA/480 s, 30 mA/240 s, respectively. A thin Pt-layer is sputtered (40mA/4min) at the bottom surface of the specimens to serve as a counter electrode.

Selection of microelectrode material:

Selection for microelectrodes material is a critical aspect, as it was experimentally verified (in this work) that *PVD* sputtered platinum (Pt) microelectrodes provide a large dominating Schottky barrier response while no dislocation/bulk response can be detected. In contrast, for Aluminum-Gold (Al-Au) microelectrodes, dislocation and bulk response can be fittingly measured, while no Schottky barrier response was detected within the measured frequency range. However, experimental data beyond 100 °C was not plausible as the non-reproducible defect chemical states were observed from 110 °C onwards (experimentally established in this work). Besides, *PVD* sputtered Al-Au microelectrodes get oxidized above 120 °C.

GIS-deposition of microelectrodes:

Electron beam assisted-gas injection system (GIS; Zeiss Auriga, Germany) technique was employed inside an SEM (Zeiss Auriga, Germany) to furnish tungsten microelectrodes to extremely small regions. A 20 kV electron beam continuously scanned a selected area of the surface (3x3 µm^2) while the valve of GIS system was opened for an optimized time of 120 seconds. The image drift was avoided by placing silver paint onto the sample surface in the vicinity of the selected area. GIS deposited microelectrodes were also furnished onto recovered zone (low dislocation density) (E_{GIS-1}) and bundled regions with medium (E_{GIS-2}) and high dislocation density (E_{GIS-3}) for comparison. MCIS measurements were performed onto GIS deposited microelectrodes *via* Hioki impedance analyzer (Hioki Europe GmbH, Eschborn, Germany) at room temperature in the frequency range of 100 Hz to 200 kHz with an amplitude of 1V.

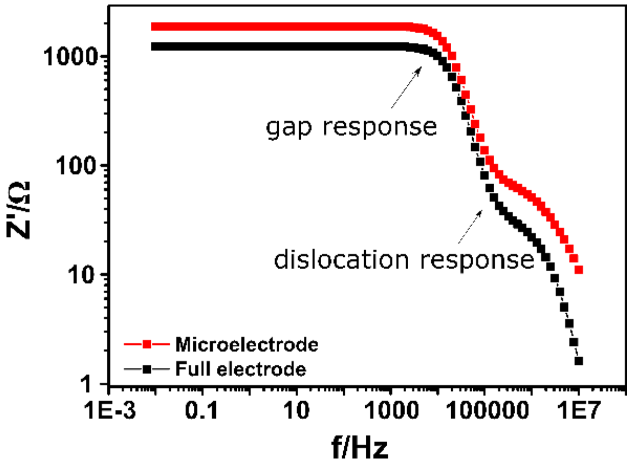

Fig. S2. Comparison of simulated real part impedance (Z') for full and microelectrode measurements. Real part of impedance data from simulations with dislocations using a 20 µm microelectrode or full electrode coverage in a Bode-plot. The first bend of the curve at low frequency (from left to right) depicts the response from the gap, and the second bend (higher frequency) shows the response from the dislocations. It can be seen that with full electrode measurements, mostly the gap response dominates. While for the microelectrodes, dislocation response is more dominant.

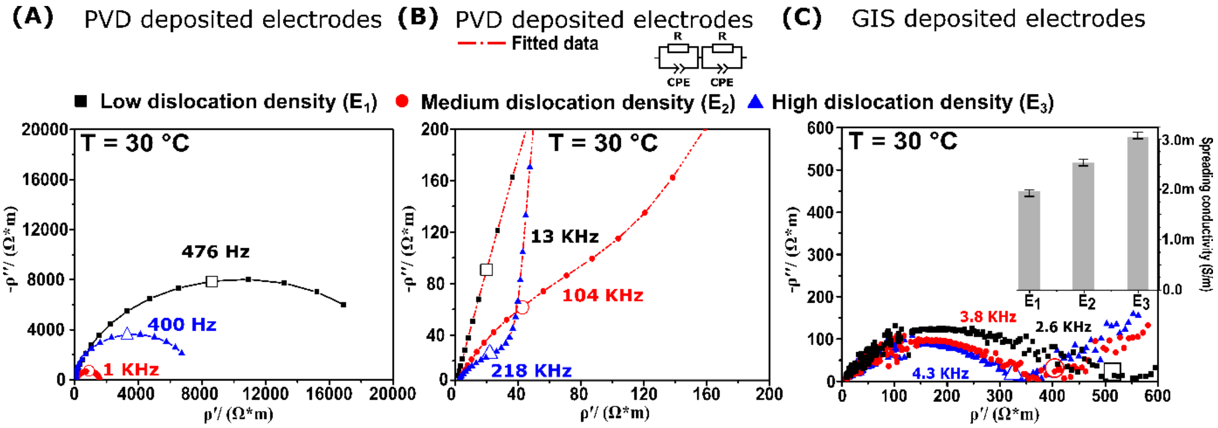

Fig. S3. Comparison of resistivity for PVD and GIS deposited electrodes. Nyquist plots of the resistivity from impedance spectra for PVD and GIS deposited electrodes. Resistivity values for both measurements follow a similar trend.

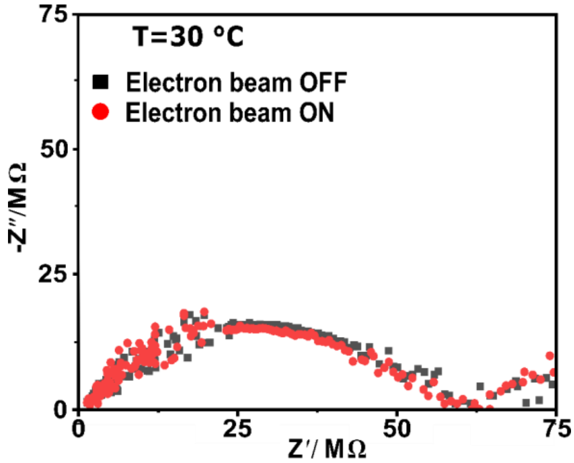

Fig. S4. Impact of SEM environment on GIS deposited microelectrode measurements. Characteristic impedance spectra of a GIS deposited electrode measured inside the SEM chamber with electron beam ON/OFF. No appreciable difference was observed. This warrants reliable measurements inside the SEM chamber.